Self-consistent embedding theory for locally correlated configuration interaction wave functions in condensed matter

Patrick Huang and Emily A. Carter[a)]
Department of Mechanical and Aerospace Engineering and Program in Applied and Computational Mathematics, Princeton University, Princeton, New Jersey 08544-5263

(Received 31 May 2006; accepted 19 July 2006; published online 23 August 2006)

We present new developments on a density-based embedding strategy for the electronic structure of localized feature in periodic, metallic systems [see T. Klüner *et al.*, J. Chem. Phys. **116**, 42 (2002), and references therein]. The total system is decomposed into an embedded cluster and a background, where the background density is regarded as fixed. Its effect on the embedded cluster is modeled as a one-electron potential derived from density functional theory. We first discuss details on the evaluation of the various contributions to the embedding potential and provide a strategy to incorporate the use of ultrasoft pseudopotentials in a consistent fashion. The embedding potential is obtained self-consistently with respect to both the total and embedded cluster densities in the embedding region, within the framework of a frozen background density. A strategy for accomplishing this self-consistency in a numerically stable manner is presented. Finally, we demonstrate how dynamical correlation effects can be treated within this embedding framework via the multireference singles and doubles configuration interaction method. Two applications of the embedding theory are presented. The first example considers a Cu dimer embedded in the (111) surface of Cu, where we explore the effects of different models for the kinetic energy potential. We find that the embedded Cu density is reasonably well-described using simple models for the kinetic energy. The second, more challenging example involves the adsorption of Co on the (111) surface of Cu, which has been probed experimentally with scanning tunneling microscopy [H. C. Manoharan *et al.*, Nature (London) **403**, 512 (2000)]. In contrast to Kohn-Sham density functional theory, our embedding approach predicts the correct spin-compensated ground state. © *2006 American Institute of Physics*. [DOI: 10.1063/1.2336428]

I. INTRODUCTION

Accurate methods for the electronic structure of condensed phases are a topic of intense activity in chemistry and physics. Among the most successful methods to date are those based on density functional theory (DFT),[1,2] in which the electron density ρ is regarded as the central variational quantity of interest. Despite the fact that the knowledge of exact DFT functionals is incomplete, DFT still enjoys widespread popularity because it provides a good balance between computational effort and accuracy. However, there are a number of well-known situations where DFT is inadequate: strongly correlated systems, excited states, and open-shell systems, just to name a few. While there exist established methods to deal with these cases in finite systems, i.e., molecules and small clusters, these methods typically cannot be applied to condensed phases in a straightforward manner.

We are interested in situations where the system's electronic structure consists of a localized feature in a metallic crystal, e.g., an impurity, vacancy, adsorbate, etc. A logical way to proceed is to identify a chemically active region centered around the feature of interest and to focus the modeling effort there.[3,4] The most basic model is simply to consider a bare cluster carved out from the bulk. This strategy has been successful in studying the reconstruction of Si surfaces and the adsorption of atoms and small molecules on Si surfaces.[5–9] Removing a subunit from a covalently bonded solid gives a truncated cluster with dangling bonds, which can be dealt with by terminating the cluster with saturating atoms such as H. Models in which the cluster under consideration is embedded in a background of point charges can provide a reasonable description of ionic crystals.[10,11]

More sophisticated approaches incorporate some sort of a quantum mechanical description of the background and its coupling to the local feature of interest. One class of methods[12–16] begins with the defect-free host system as reference, whose Hartree-Fock or DFT (i.e., single-determinant wave function) solution is readily available. The defect and its influence on the surroundings are viewed as a perturbation on the ideal host. The one-electron Green's function for the full system is solved for in terms of the Green's function for the unperturbed host and a perturbing potential localized within the embedded region.

A somewhat different embedding strategy, which can be traced back to Whitten[17,18] begins by finding a single-determinant wave function solution for a large, finite cluster. A localization scheme is applied to produce a set of one-electron orbitals localized at the region of interest, and a set associated with the background. The background orbitals are used to construct effective Coulomb and exchange operators that act on electrons in the embedded region. Processes such

[a)]Electronic mail: eac@princeton.edu

as chemisorption can be studied by forming explicitly correlated (multiconfigurational) wave functions built from the set of orbitals localized in the embedded region. Subsequent workers have also extended this approach to periodic systems.[19]

The examples outlined above require a partitioning of the one-electron orbitals for the total system into a distinct subspace that spans the embedded region and a complementary subspace that spans the background. Such a transformation can usually be made for molecules, small clusters, and insulating systems, whose first-order reduced density matrix decays exponentially with respect to distance $|\mathbf{r}-\mathbf{r}'|$. The difficulty with metallic or zero-band-gap systems is that their density matrices decay algebraically, thus making it difficult to construct distinct, localized subspaces for occupied and virtual orbitals. In other words, conduction electrons in metallic systems are simply too delocalized to apply a partitioning in orbital space. Gutdeutsch *et al.* have provided a careful examination of issues related to orbital localization.[20,21]

An alternative formulation of the embedding problem can be made based on ideas from DFT, where the partitioning is done in real space in terms of charge densities, thus avoiding the difficulties mentioned above with orbital localization. It is along these lines that our current work follows. The basic idea is due to Cortona,[22] who proposed a strategy to reduce a DFT calculation for a periodic crystal to that of a single atom in the presence of an effective background potential. This potential is a functional of the density and is obtained self-consistently with respect to the atom density. Wesolowski and Warshel[23] have adopted these ideas to examine a model solvation problem, where they apply a DFT treatment of a solute molecule in the presence of an effective potential representing the solvent background. Later workers have expanded on this model to include a time-dependent DFT treatment of the solute to obtain solvatochromic shifts.[24,25] Stefanovich and Truong have adopted Cortona's strategy to examine the adsorption of water on the surface of NaCl(001), incorporating a background of point charges to reproduce the correct Madelung potential.[26] Recently, Choly *et al.* have coupled a DFT region to a classical description of the background, for use in a quantum mechanics/molecular mechanics (QM/MM)-type simulation of simple metals.[27] In all these examples, the embedded region of interest is described with DFT, and one of the strengths of this strategy is an effective reduction of the size of the problem.

In this work, we build upon a density-based embedding theory developed in a series of papers from our group,[28–32] which is suitable for metallic crystals. A distinguishing feature of our approach is that we replace the DFT treatment of the embedded region with an *ab initio* wave function treatment, thus allowing us to handle situations where DFT is not applicable. This introduces additional complications, however, due to the need to match an *ab initio* description based on wave functions constructed from atom-centered basis sets, and a periodic DFT description based on a plane-wave basis sets. In particular, this raises issues about the choice of pseudopotentials, which is one topic of discussion in this paper.

The basic quantity in the theory is the embedding potential v_{emb}, which is derived from DFT considerations. In previous implementations,[28–32] the procedure began with a periodic DFT calculation for the total system density ρ. The quantity ρ was regarded as fixed in the embedding model and was used to construct the embedding potential v_{emb}. The embedded cluster density in the presence of v_{emb} was found using *ab initio* methods, and the cluster calculations were repeated until self-consistency was achieved between v_{emb} and the density for the embedded region. Here, we take a different view in that we regard the background density as fixed, instead of the total system density ρ. This is a more physically appealing approach, since the embedding theory is meant to deal with situations where the important electron correlation effects are localized within the cluster region of interest, while the background remains relatively inert. Releasing the constraint on the total density ρ also solves the numerical issues encountered in previous efforts,[28–32] which prevented a solution for a fully self-consistent v_{emb}.

We begin with an overview of the embedding formalism in Sec. II, with particular emphasis on how the various contributions to the embedding potential are evaluated, including use of a fully self-consistent embedding potential. We discuss in detail the issues that arise when pseudopotentials are employed to represent the atomic cores and our strategy for a consistent pseudopotential model. In Sec. III, we examine a Cu dimer embedded in the (111) surface of Cu, in which both the embedded subsystem and background are described with DFT. This example of DFT-in-DFT embedding explores the effects of different kinetic energy functionals[32] and shows that simple models can yield reasonable densities. The second example of Sec. IV examines the adsorption of a single magnetic adatom on a nonmagnetic, metallic surface, namely, Co on Cu(111). This case is known to be a strongly correlated system exhibiting the Kondo effect, in which the conduction electrons of the nonmagnetic background align their spins to screen out the spin moment localized on the magnetic impurity.[33] Co on Cu(111) is one of the first systems in which the Kondo effect due to a *single* impurity was probed,[34,35] thus raising new interest in the electronic structure of this Kondo state. Here we utilize self-consistent embedded multireference singles and doubles configuration interaction (MRSDCI) calculations to describe the many-body correlations of the Kondo state.

All plane-wave DFT calculations reported in this work are performed using the CASTEP code,[36] while the *ab initio* calculations are done with the MOLCAS package,[37] modified for use with the embedding.

II. THEORY

Consider a partitioning of the total system density ρ into an embedded cluster density ρ_{I} and background density ρ_{II}. The total system energy $E[\rho]$ formally can be decomposed as

$$E[\rho] = E_{\mathrm{I}}[\rho_{\mathrm{I}}] + E_{\mathrm{II}}[\rho_{\mathrm{II}}] + E_{\mathrm{int}}, \tag{1}$$

where E_{I} is the energy associated with the embedded cluster, E_{II} is the energy due to the background, and E_{int} is a cluster-background interaction energy. Since $\rho=\rho_{\mathrm{I}}+\rho_{\mathrm{II}}$, we choose the independent variables to be ρ and ρ_{I}. Assuming the back-

ground region is large enough such that $\delta E_{\mathrm{II}}/\delta\rho_{\mathrm{I}} \approx 0$, variation of $E[\rho]$ with respect to ρ and ρ_{I} leads to the Euler equations

$$\frac{\delta E[\rho]}{\delta\rho} = 0, \tag{2}$$

$$\frac{\delta E_{\mathrm{I}}[\rho_{\mathrm{I}}]}{\delta\rho_{\mathrm{I}}} + v_{\mathrm{emb}} = 0, \tag{3}$$

where $v_{\mathrm{emb}} = \delta E_{\mathrm{int}}/\delta\rho_{\mathrm{I}}$. The solution of Eq. (2) is the density ρ which minimizes the total energy, while the solution of Eq. (3) is the density ρ_{I} which minimizes the energy of the embedded cluster, in the presence of an effective potential v_{emb}. Given a specification for v_{emb}, the idea is to begin with some approximate method for Eq. (2) which is appropriate for periodic crystals, e.g., plane-wave DFT with an approximate treatment of exchange-correlation. The finite cluster problem posed by Eq. (3) is treated with some higher-level theory drawn from a well-established hierarchy of *ab initio* quantum chemistry methods.

This embedding theory essentially centers on the choice for the potential, v_{emb}. A DFT-based model is adopted for v_{emb} by expressing E_{int} as[28,29]

$$E_{\mathrm{int}} = E[\rho] - E_{\mathrm{I}}[\rho_{\mathrm{I}}] - E_{\mathrm{II}}[\rho_{\mathrm{II}}], \tag{4}$$

where the energy functionals $E_i[\rho_i]$ (i=total, I, II) are explicitly defined in the usual DFT sense as

$$E_i[\rho_i] = T_s[\rho_i] + J[\rho_i] + E_{\mathrm{xc}}[\rho_i] + \int d\mathbf{r}\rho_i(\mathbf{r})v^i_{\mathrm{ion}}(\mathbf{r}). \tag{5}$$

Here, T_s, J, and E_{xc} are the kinetic, Hartree, and exchange-correlation energies, respectively, and v^i_{ion} is the electron-ion potential due to atoms in region i (i=total, I, II). Taking the functional derivative of Eq. (4) with respect to $\rho_{\mathrm{I}}(\mathbf{r})$ gives

$$v_{\mathrm{emb}} = \frac{\delta E_{\mathrm{int}}}{\delta\rho_{\mathrm{I}}(\mathbf{r})} \tag{6}$$

$$= \int d\mathbf{r}' \frac{\delta E[\rho]}{\delta\rho(\mathbf{r}')}\frac{\delta\rho(\mathbf{r}')}{\delta\rho_{\mathrm{I}}(\mathbf{r})} - \frac{\delta E_{\mathrm{I}}[\rho_{\mathrm{I}}]}{\delta\rho_{\mathrm{I}}(\mathbf{r})} - \frac{\delta E_{\mathrm{II}}[\rho_{\mathrm{II}}]}{\delta\rho_{\mathrm{I}}(\mathbf{r})}, \tag{7}$$

where the first term comes from the usual chain rule for functional derivatives. Since $\rho(\mathbf{r}) = \rho_{\mathrm{I}}(\mathbf{r}) + \rho_{\mathrm{II}}(\mathbf{r})$, the functional derivative $\delta\rho(\mathbf{r}')/\delta\rho_{\mathrm{I}}(\mathbf{r})$ in the integrand above must be zero unless $\mathbf{r}=\mathbf{r}'$, and the integral becomes

$$\int d\mathbf{r}' \frac{\delta E[\rho]}{\delta\rho(\mathbf{r}')}\frac{\delta\rho(\mathbf{r}')}{\delta\rho_{\mathrm{I}}(\mathbf{r})} = \int d\mathbf{r}' \frac{\delta E[\rho]}{\delta\rho(\mathbf{r}')}\delta(\mathbf{r}-\mathbf{r}') = \frac{\delta E[\rho]}{\delta\rho(\mathbf{r})}. \tag{8}$$

If we again assume that $\delta E_{\mathrm{II}}/\delta\rho_{\mathrm{I}} \approx 0$, this leads to a one-electron embedding potential v_{emb} of the form

$$v_{\mathrm{emb}} = \frac{\delta E[\rho]}{\delta\rho} - \frac{\delta E_{\mathrm{I}}[\rho_{\mathrm{I}}]}{\delta\rho_{\mathrm{I}}}. \tag{9}$$

Substituting Eq. (5) for $E[\rho]$ and $E_{\mathrm{I}}[\rho_{\mathrm{I}}]$ above, the potential v_{emb} can also be organized into terms due to the kinetic, Hartree, exchange-correlation, and electron-ion contributions:

$$v_{\mathrm{emb}} = v_{T_s} + v_J + v_{\mathrm{xc}} + v_{\mathrm{ion}}, \tag{10}$$

where the individual terms are

$$v_{T_s} = \frac{\delta T_s[\rho]}{\delta\rho} - \frac{\delta T_s[\rho_{\mathrm{I}}]}{\delta\rho_{\mathrm{I}}}, \tag{11}$$

$$v_J = \frac{\delta J[\rho]}{\delta\rho} - \frac{\delta J[\rho_{\mathrm{I}}]}{\delta\rho_{\mathrm{I}}}, \tag{12}$$

$$v_{\mathrm{xc}} = \frac{\delta E_{\mathrm{xc}}[\rho]}{\delta\rho} - \frac{\delta E_{\mathrm{xc}}[\rho_{\mathrm{I}}]}{\delta\rho_{\mathrm{I}}}, \tag{13}$$

$$v_{\mathrm{ion}} = v^{\mathrm{II}}_{\mathrm{ion}}. \tag{14}$$

$v^{\mathrm{II}}_{\mathrm{ion}}$ is the electron-ion potential due to the background atoms alone. The explicit functional forms of these terms and the details regarding their evaluation are given in following subsections.

In principle, Eqs. (2) and (3) should be solved simultaneously for ρ and ρ_{I}; however, they are treated with very different methodologies, and it is not clear how to satisfy both conditions in a self-consistent manner. We adopt here a scheme which begins with separate plane-wave DFT calculations for the total system, ρ, and the *isolated* cluster of interest, $\rho^{\mathrm{bare}}_{\mathrm{I}}$. An estimate for the background density ρ_{II} is obtained as $\rho_{\mathrm{II}} = \rho - \rho^{\mathrm{bare}}_{\mathrm{I}}$ and is regarded as fixed throughout the embedding model. This leaves an essentially empty embedded region to be "filled in" with an *ab initio* theory of choice and an appropriate set of *ab initio* pseudopotentials to represent the embedded ions. An initial guess for the embedding potential is evaluated as $v_{\mathrm{emb}}[\rho, \rho^{\mathrm{bare}}_{\mathrm{I}}]$, and a new cluster density ρ'_{I} in the presence of this potential is found. The new cluster density ρ'_{I} is added to the frozen background density to yield an updated total system density $\rho' = \rho'_{\mathrm{I}} + \rho_{\mathrm{II}}$ and updated embedding potential $v_{\mathrm{emb}}[\rho', \rho'_{\mathrm{I}}]$. The cycle is then repeated until a self-consistent ground state cluster density $\hat{\rho}_{\mathrm{I}}$ and potential $v_{\mathrm{emb}}[\hat{\rho}, \hat{\rho}_{\mathrm{I}}]$ are found. Excited state calculations for the embedded cluster are subsequently performed using this converged, self-consistent potential $v_{\mathrm{emb}}[\hat{\rho}, \hat{\rho}_{\mathrm{I}}]$.

While our choice for ρ_{II} is not guaranteed to be positive everywhere, this is not an issue in practice. First of all, the quantity ρ_{II} is never used alone, for the embedding potential v_{emb} is a functional of the cluster density ρ'_{I} and total density $\rho' = \rho'_{\mathrm{I}} + \rho_{\mathrm{II}}$. Of course, the method can fail for a poor choice of ρ_{II}, and therefore ρ_{II} must be chosen appropriately. Here, the DFT bare cluster density $\rho^{\mathrm{bare}}_{\mathrm{I}}$ used to obtain $\rho_{\mathrm{II}} = \rho - \rho^{\mathrm{bare}}_{\mathrm{I}}$ is computed in a manner very similar to the computation for the DFT total density ρ: same basis sets, same pseudopotentials, etc. The cancellation between $\rho^{\mathrm{bare}}_{\mathrm{I}}$ and ρ is close within the embedded region, while at the cluster boundary $\rho^{\mathrm{bare}}_{\mathrm{I}}$ decays to zero.

We also point out that this scheme yields a fully self-consistent embedding potential, in contrast with previous implementations of the embedding theory,[28–32] where the total system density ρ is frozen. Fixing ρ instead of the background region ρ_{II} leads to numerical problems in the evaluation and update of embedding potential. This issue will be discussed further in the example given in Sec. III. For the

frozen background approximation to be valid, however, the effects of the inhomogeneity of interest should be contained entirely within the embedded region. Therefore, one should proceed cautiously in situations where a significant polarization of the background is expected (e.g, charge transfer processes, etc.). Also, in this model, the *ab initio* treatment of the embedded region will produce a wave function localized there. Previous work employed the use of ghost functions at the cluster boundary,[29] but later work suggested the effects were small.[32]

The remainder of this section will be concerned with the details in the implementation of the theory, namely, the evaluation of the various potential terms which enter into the embedding model.

A. Embedding potential

The plane-wave DFT calculations provide a density evaluated on a uniform grid, whose resolution is controlled by the plane-wave kinetic energy cutoff. All local terms in the embedding potential are thus obtained on this grid in real space. Matrix elements with respect to a Gaussian-type basis set are evaluated numerically, i.e.,

$$\langle \chi_m^A | v_{\mathrm{emb}} | \chi_n^B \rangle = \Delta V \sum_i \chi_m(\mathbf{r}_i - \mathbf{r}_A) v_{\mathrm{emb}}(\mathbf{r}_i) \chi_n(\mathbf{r}_i - \mathbf{r}_B), \quad (15)$$

where ΔV is the grid volume element, χ_m^A, χ_n^B are Gaussian-type functions centered at $\mathbf{r}_A, \mathbf{r}_B$, and the summation runs over all points on the real space grid. The only nonlocal contributions to the embedding potential come from the nonlocal terms in the pseudopotentials (Sec. II B) and are independent of the density. These integrals can be reduced to a one-dimensional, atom-centered quadrature, which is described in Sec. II A 3. We discuss here the various contributions to the embedding potential, Eqs. (10)–(14), and the details involved in their evaluation.

1. Kinetic energy contribution

We consider two classes of models for the kinetic energy potential $\delta T_s / \delta \rho_i$, where ρ_i refers to the total density ρ or the embedded cluster ρ_{I}. The same model potential is used for all regions, and so the subscript i is dropped here. The first class of models is the Thomas-Fermi λ-von Weizsäcker functional,[38]

$$T_s[\rho] = T_{\mathrm{TF}}[\rho] + \lambda T_{\mathrm{vW}}[\rho], \quad (16)$$

$$\frac{\delta T_s}{\delta \rho} = \frac{\delta T_{\mathrm{TF}}}{\delta \rho} + \lambda \frac{\delta T_{\mathrm{vW}}}{\delta \rho}, \quad (17)$$

where T_{TF} is the Thomas-Fermi functional,

$$T_{\mathrm{TF}}[\rho] = C_F \int d\mathbf{r} \rho^{5/3}(\mathbf{r}), \quad (18)$$

$$\frac{\delta T_{\mathrm{TF}}}{\delta \rho} = \frac{5}{3} C_F \rho^{2/3}(\mathbf{r}), \quad (19)$$

and $C_F = \frac{3}{10}(3\pi^2)^{2/3}$. T_{vW} is the von Weizsäcker functional,

$$T_{\mathrm{vW}}[\rho] = \frac{1}{8} \int d\mathbf{r} \frac{|\nabla \rho(\mathbf{r})|^2}{\rho(\mathbf{r})}, \quad (20)$$

$$\frac{\delta T_{\mathrm{vW}}}{\delta \rho} = -\frac{1}{2} \frac{\nabla^2 \rho^{1/2}(\mathbf{r})}{\rho^{1/2}(\mathbf{r})}. \quad (21)$$

Common choices for the parameter λ include $\lambda = 1/9$, as derived from the conventional gradient expansion,[38] or $\lambda = 1/5$ based on fitting to exact quantum solutions for hydrogenic atoms, i.e., no electron-electron interactions.[39] The Thomas-Fermi term T_{TF} is evaluated in real space, while the Laplacian factor in the von Weizsäcker term T_{vW} is evaluated using fast Fourier transforms (FFTs), for potentials involving both ρ and ρ_{I}.

Numerical evaluation of the von Weizsäcker potential is problematic, leading to spurious divergences near the atomic cores. This issue was analyzed by Klüner *et al.*,[32] who showed that this divergence is an artifact arising from the use of pseudopotentials. In short, the conventional gradient expansion leading to the von Weizsäcker term should only be applied when $|\nabla \rho| / k_F \rho \ll 1$, where k_F is the Fermi wave vector $k_F = (3\pi^2 \rho)^{1/3}$.[1] Following Klüner *et al.*, we apply a truncation scheme to the kinetic energy potential as

$$\frac{\delta T_s}{\delta \rho} = \begin{cases} v_{\mathrm{TF}} + \lambda v_{\mathrm{vW}} & \text{if } \left| \dfrac{v_{\mathrm{vW}}}{v_{\mathrm{TF}}} \right| \leq 1 \\ v_{\mathrm{TF}} & \text{if } \left| \dfrac{v_{\mathrm{vW}}}{v_{\mathrm{TF}}} \right| > 1, \end{cases} \quad (22)$$

where v_{TF} is the Thomas-Fermi potential of Eq. (19) and v_{vW} is the von Weizsäcker potential of Eq. (21).

The second class of kinetic energy potentials we explore involves orbital-dependent functionals. The Kohn-Sham DFT calculations yield a set of orbitals $\{\psi_{\mathbf{k}s}\}$ and the density $\rho(\mathbf{r}) = \Sigma_{\mathbf{k}s} |\psi_{\mathbf{k}s}(\mathbf{r})|^2$, where $\mathbf{k}$ and s are indices for bands and spin, respectively. While the noninteracting kinetic energy $T_s[\{\psi_{\mathbf{k}s}\}]$ is given by

$$T_s[\{\psi_{\mathbf{k}s}\}] = -\tfrac{1}{2} \sum_{\mathbf{k}s} \langle \psi_{\mathbf{k}s} | \nabla^2 | \psi_{\mathbf{k}s} \rangle, \quad (23)$$

its functional derivative with respect to the density, $\delta T_s / \delta \rho$, is not well defined because the Kohn-Sham orbitals $\{\psi_{\mathbf{k}s}\}$ are not unique. However, if it is assumed that $T_s[\{\psi_{\mathbf{k}s}\}]$ is a linear functional of the density ρ, then the functional derivative should obey

$$\int d\mathbf{r} \rho(\mathbf{r}) \frac{\delta T_s}{\delta \rho} = T_s[\{\psi_{\mathbf{k}s}\}]. \quad (24)$$

In more realistic situations, $T_s[\{\psi_{\mathbf{k}s}\}]$ is not expected to be a linear functional of ρ. Thus, we consider a potential of the form

$$\frac{\delta T_s}{\delta \rho} = -\frac{1}{2} \gamma \frac{\sum_{\mathbf{k}s} \psi_{\mathbf{k}s}^*(\mathbf{r}) \nabla^2 \psi_{\mathbf{k}s}(\mathbf{r})}{\rho(\mathbf{r})}, \quad (25)$$

which satisfies Eq. (24) when $\gamma = 1$. The parameter γ is regarded as an adjustable parameter which approximately takes into account any nonlinearities in $T_s[\{\psi_{\mathbf{k}s}\}]$.

In an ultrasoft calculation, the Kohn-Sham wave functions $\{\psi_{\mathbf{k}s}\}$ are not properly norm conserving, and the full charge density includes an additional contribution from the augmentation density, Eq. (38). This augmentation density is strictly localized within the augmentation region around an atom, while the density outside of these regions is given by the usual $\Sigma_{\mathbf{k}s}|\psi_{\mathbf{k}s}(\mathbf{r})|^2$. Thus, Eq. (25) is only well defined outside the augmentation region. In this case, a simple strategy is to adopt a hybrid model for the kinetic energy, in which the potential within the augmentation regions is taken to be the Thomas-Fermi potential, Eq. (19). The potential outside of the augmentation regions remains that given by the orbital-based model, Eq. (25).

2. Electron-electron contributions: Hartree and exchange-correlation

The Hartree energy and potential are given by

$$J[\rho] = \int d\mathbf{r} d\mathbf{r}' \frac{\rho(\mathbf{r})\rho(\mathbf{r}')}{|\mathbf{r}-\mathbf{r}'|}, \tag{26}$$

$$\frac{\delta J}{\delta \rho} = \int d\mathbf{r}' \frac{\rho(\mathbf{r}')}{|\mathbf{r}-\mathbf{r}'|}. \tag{27}$$

The Hartree interaction is long ranged and should be handled with care. It is most straightforward to deal with this term in Fourier space,

$$\frac{\delta J}{\delta \rho} = \frac{4\pi}{V} \sum_{\mathbf{G}\neq 0} \frac{\tilde{\rho}(\mathbf{G})}{|\mathbf{G}|^2} e^{i\mathbf{G}\cdot\mathbf{r}}, \tag{28}$$

where V is the real space unit cell volume, $\mathbf{G}$ is a reciprocal space vector, and $\tilde{\rho}(\mathbf{G})$ is the Fourier transform of $\rho(\mathbf{r})$. The summation runs over all reciprocal space vectors except for $\mathbf{G}=0$, which exactly cancels with the $\mathbf{G}=0$ component of the electron-ion interaction, in the case of a neutral system. The Hartree potential associated with the embedded cluster, $\delta J/\delta \rho_{\mathrm{I}}$, is also evaluated in the same manner.

We employ the local density approximation[40,41] (LDA) for the exchange-correlation potential $\delta E_{\mathrm{xc}}/\delta\rho$, consistent with the choice of exchange-correlation in the plane-wave DFT calculations and the pseudopotential generation. This term is short ranged and readily evaluated in real space.

3. Electron-ion contribution

The electron-ion potential $v_{\mathrm{ion}}^{\mathrm{II}}$ consists of contributions from the background atom pseudopotentials (Sec. II B),

$$\begin{aligned} v_{\mathrm{ion}}^{\mathrm{II}} &= \sum_A v_{\mathrm{ps}}(|\mathbf{r}-\mathbf{r}_A|) \\ &= \sum_A v_{\mathrm{loc}}(|\mathbf{r}-\mathbf{r}_A|) \\ &\quad + \sum_A \sum_{ij} D_{ij}^{(0)} |\beta_i^A\rangle\langle\beta_j^A|, \end{aligned} \tag{29}$$

where the summation runs over the background atoms only β_i^A and β_j^A refer to projectors centered at $\mathbf{r}_A$ and $D_{ij}^{(0)}$ are projector weights. Details on the construction of these quantities are discussed in Sec. II B. The purely local part is long ranged and thus evaluated in Fourier space,

TABLE I. Cu pseudo-wave-function cutoff radii r_c and reference energies ϵ_i for each angular momentum channel l. The label (a.e.) in the entries under ϵ_i denotes self-consistent eigenenergies of the all-electron atom. The $l=1$ channel is used to construct the local potential v_{loc}.

l	r_c (a_0)	ϵ_i(a.u.)
0	2.6	−0.172 34 (a.e.)
0	2.6	0.0
1 (loc)	2.6	0.0
2	2.0	−0.202 19 (a.e.)
2	2.0	−0.175

$$\sum_A v_{\mathrm{loc}}(|\mathbf{r}-\mathbf{r}_A|) = \frac{1}{V} \sum_{\mathbf{G}\neq 0} S(\mathbf{G}) \tilde{v}_{\mathrm{loc}}(|\mathbf{G}|) e^{i\mathbf{G}\cdot\mathbf{r}}, \tag{30}$$

where V is the real space unit cell volume, $\mathbf{G}$ is a reciprocal space vector, $\tilde{v}_{\mathrm{loc}}(|\mathbf{G}|)$ is the Fourier transform of the local potential $v_{\mathrm{loc}}(|\mathbf{r}|)$, and $S(\mathbf{G})$ is the structure factor associated with the background atoms,

$$S(\mathbf{G}) = \sum_A e^{-i\mathbf{G}\cdot\mathbf{r}_A}. \tag{31}$$

The summation runs over all $\mathbf{G}$ except for $\mathbf{G}=0$, which exactly cancels the $\mathbf{G}=0$ component of the Hartree potential.

The nonlocal part of the electron-ion potential is short ranged and strictly localized within the cutoff radii r_c (Table I, discussed below). To obtain matrix elements with respect to a Gaussian-type basis set χ_m^B, χ_n^C, we need the two-center integrals $\langle\chi_m^B|\beta_i^A\rangle, \langle\beta_j^A|\chi_n^C\rangle$. These integrals are evaluated in real space, where the angular integration is done analytically,[42,43] leaving a radial integral which is done numerically.

B. Pseudopotentials

The embedding strategy we present proceeds in two distinct steps: plane-wave Kohn-Sham DFT calculations for a periodic crystal and *ab initio* cluster calculations for the localized region of interest, in the presence of an effective embedding potential v_{emb}. The second step requires data from the first step as input. In particular, we use pseudopotentials to represent the interaction of the valence electrons with the core electrons and nuclei. A pseudopotential model that is appropriate for the methodology at hand must be chosen for each step of the calculation, yet it should employ approximations that are consistent across the various levels of theory. In the DFT calculations for the total density ρ, one should use DFT pseudopotentials that are generated and unscreened with the same approximation for exchange-correlation as that used in the valence-only calculations. In the *ab initio* cluster calculations, the embedded atoms should instead be represented with effective core potentials (ECPs) derived from Hartree-Fock theory,[44] since the *ab initio* methods we use here are based on wave functions that are supersets of Hartree-Fock theory. By contrast, the background atoms enter into the embedded cluster calculations via the electron-ion contribution to the embedding potential, $v_{\mathrm{ion}}^{\mathrm{II}}$, and should be represented using a set of DFT pseudopotentials that can be used in both the plane-wave DFT and the *ab*

initio calculations, since they appear in both. The background atom pseudopotentials must be consistent with the background electron density, which is derived from DFT.

Generally speaking, solid-state DFT pseudopotentials can be classified as one of the two types: norm-conserving[45,46] or ultrasoft.[47,48] The form of norm-conserving pseudopotentials (NCPs) is consistent with the effective core potential (ECP) model[44] commonly utilized in molecular calculations, and so they can be incorporated into existing quantum chemistry packages for use. This was done in the previous embedding work of Refs. 28–32, where a NCP used for solid-state calculations was mapped onto the ECP form. However, plane-wave methods that use norm-conserving potentials to model transition metals typically require very large basis sets, due to the large number of plane waves needed to describe sharply peaked *d*-electron densities. While this does not pose a difficulty in *ab initio* calculations, which use localized Gaussian-type basis sets, it did cause the previous embedding work to be rather expensive.

The expense of plane-wave DFT calculations was largely remedied through the development of ultrasoft pseudopotentials,[47,48] which allows for the use of plane-wave basis sets with much smaller kinetic energy cutoff values. The basic idea is to separate out a "hard" part of the electron density that is strictly localized within the atomic core regions, leaving behind a "soft" density. The Kohn-Sham DFT equations are then solved using a double-grid implementation,[48] in which most of the numerical effort is spent on a coarse reciprocal space grid representing the soft part of the wave function, with relatively fewer operations involving the hard part, which is represented on a denser grid. The computational savings afforded by this strategy can be significant, but this comes at the expense of a more complex formalism which is not easily implemented in *ab initio* cluster calculations.

In order to combine the advantages of these two formulations, our approach is to generate a norm-conserving pseudopotential for the background ions and construct a modified ultrasoft pseudopotential which reproduces the behavior of the associated norm-conserving pseudopotential. The cheaper ultrasoft pseudopotential is used in the plane-wave DFT calculations, while the equivalent norm-conserving pseudopotential is used in the embedded cluster calculations. In this manner, the background ions are consistently modeled across all levels of theory. A thorough discussion on pseudopotential generation can be found in Ref. 48 and will not be repeated here. Instead, we shall provide a brief review of the procedure and then describe the nonstandard features of our pseudopotentials as applied to Cu.

1. DFT pseudopotential construction

The generalized pseudopotentials in this work consist of a local part v_{loc} and nonlocal terms involving projection operators β_i and projector weights $D_{ij}^{(0)}$,[47–49]

$$v_{\mathrm{ps}} = v_{\mathrm{loc}}(r) + \sum_{ij} D_{ij}^{(0)} |\beta_i\rangle\langle\beta_j|. \tag{32}$$

The construction of the individual β_i and $D_{ij}^{(0)}$ can be done using a norm-conserving or ultrasoft scheme. Its generation

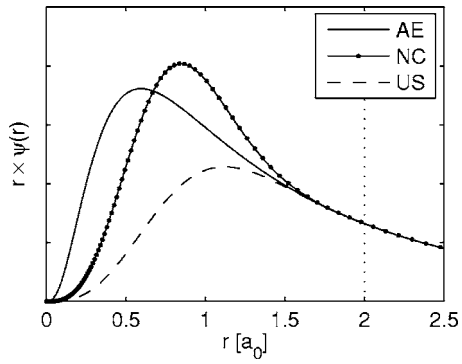

FIG. 1. Cu all-electron (AE), norm-conserving (NC), and ultrasoft (US) radial wave functions for the $l=2$ angular momentum channel (fourth line of Table I). The cutoff radius is defined at $r_c=2a_0$.

begins by choosing a reference electronic configuration for the atomic species of interest and finding the self-consistent solution to the all-electron (AE) DFT equation:

$$[T + V^{\mathrm{AE}}(r)]\psi_i^{\mathrm{AE}}(\mathbf{r}) = \epsilon_i^{\mathrm{AE}}\psi_i^{\mathrm{AE}}(\mathbf{r}). \tag{33}$$

Here, T is the kinetic energy operator, V^{AE} is the usual Kohn-Sham effective potential for the all-electron atom, and ϵ_i^{AE} and ψ_i^{AE} are the eigenenergies and eigenfunctions, respectively. The index i denotes a composite index $\{nlm\}$ for the radial and angular quantum numbers.

For each angular momentum channel l, a few (typically one to two) reference energies ϵ_i are chosen around the range where band formation is expected. Holding V^{AE} fixed, the wave function $\psi_i(\mathbf{r};\epsilon_i)$ at this reference energy ϵ_i is obtained as the solution of

$$[T + V^{\mathrm{AE}}(r) - \epsilon_i]\psi_i(\mathbf{r};\epsilon_i) = 0. \tag{34}$$

Note that $\psi_i(\mathbf{r};\epsilon_i)$ is not self-consistent with respect to the potential V^{AE}, except when ϵ_i is chosen to be a self-consistent eigenvalue of the atom, in which case it is simply equal to $\psi_i^{\mathrm{AE}}(\mathbf{r})$. From this point on in the text, we shall drop the parametric dependence of the wave function on ϵ_i in our notation, although its presence is implicitly assumed.

Next, a pseudo-wave-function is constructed which joins smoothly with ψ_i beyond some cutoff radius r_c. The differences between norm-conserving and ultrasoft pseudopotentials stem from additional constraints imposed (or not imposed) on the pseudo-wave-functions. Norm-conserving pseudo-wave-functions ϕ_i^{NC} also obey the generalized norm-conserving condition

$$Q_{ij}^{\mathrm{NC}} = \langle\psi_i|\psi_j\rangle - \langle\phi_i^{\mathrm{NC}}|\phi_j^{\mathrm{NC}}\rangle = 0, \tag{35}$$

while in the ultrasoft formulation, this condition is relaxed, i.e.,

$$Q_{ij}^{\mathrm{US}} = \langle\psi_i|\psi_j\rangle - \langle\phi_i^{\mathrm{US}}|\phi_j^{\mathrm{US}}\rangle \neq 0. \tag{36}$$

This provides the flexibility to construct ultrasoft pseudo-wave-functions ϕ_i^{US} which are less sharply peaked than their norm-conserving counterparts, as shown in Fig. 1. Instead, a local augmentation function $Q_{ij}^{\mathrm{US}}(\mathbf{r})$ is defined within a radial cutoff around each atom as

$$Q_{ij}^{\mathrm{US}}(\mathbf{r}) = \psi_i^*(\mathbf{r})\psi_j(\mathbf{r}) - \phi_i^{*\mathrm{US}}(\mathbf{r})\phi_j^{\mathrm{US}}(\mathbf{r}), \tag{37}$$

whose role is to make up for the charge deficit that results when $Q_{ij}^{\mathrm{US}} \neq 0$.

Given the pseudo-wave-functions ϕ_i^{NC} or ϕ_i^{US}, projector functions β_i and (unscreened) matrix elements $D_{ij}^{(0)}$ are then formed following the procedure described in Ref. 48 to yield a generalized norm-conserving or ultrasoft pseudopotential of Eq. (32). When the ultrasoft pseudopotential is used in a DFT calculation, additional terms arise in the charge density and the Kohn-Sham equations due to the presence of a nonzero $Q_{ij}^{\mathrm{US}}(\mathbf{r})$. From a set of self-consistent Kohn-Sham eigenfunctions $\{\psi_{\mathbf{k}s}\}$, the pseudo-valence-charge density in an ultrasoft calculation is evaluated as[47,48]

$$\rho(\mathbf{r}) = \sum_{\mathbf{k}s}\left[|\psi_{\mathbf{k}s}|^2 + \sum_A \sum_{ij} \langle\psi_{\mathbf{k}s}|\beta_i^A\rangle Q_{ij}^{\mathrm{US}}(\mathbf{r}-\mathbf{r}_A)\langle\beta_j^A|\psi_{\mathbf{k}s}\rangle\right]. \tag{38}$$

where the summation over A runs over ions positioned at $\mathbf{r}A$. The choice of $Q_{ij}^{\mathrm{US}}(\mathbf{r})$ made in Eq. (37) corrects the pseudo-valence density to yield an all-electron valence density. In practice, however, this is usually not the case, since the $Q_{ij}^{\mathrm{US}}(\mathbf{r})$ is typically pseudized in a way that yields a smoother augmentation charge density while preserving the total number of valence electrons.[48]

In the case of norm-conserving potentials, $Q_{ij}^{\mathrm{US}}=0$, and Eq. (38) reduces to the usual expression for the charge density $\rho(\mathbf{r})=\Sigma_{\mathbf{k}s}|\psi_{\mathbf{k}s}(\mathbf{r})|^2$. Note that unlike the situation with ultrasoft potentials, this valence density does *not* correspond to the all-electron valence density, since the core region has been pseudized away (Fig. 1) and there is no augmentation charge to make up for the difference.

2. Consistent DFT pseudopotentials: Application to Cu

The strategy we adopt to model consistently the electron-ion interaction begins by generating a norm-conserving pseudopotential for use in the *ab initio* calculations. A self-consistent solution for the all-electron, nonrelativistic DFT equation is first found for the Cu atom in the ground state $d^{10}s^1$ configuration. The local density approximation (LDA) to exchange-correlation[40,41] is employed for all pseudopotentials generated in this work, consistent with the choice of exchange-correlation in the plane-wave calculations of Sec. III and IV. Norm-conserving pseudo-wave-functions are constructed, whose values for the cutoff radii r_c and reference energies ϵ_i are summarized in Table I. The value of $r_c=2.6a_0$ for the cutoff radius corresponds approximately to the outermost peak of the all-electron $l=0$ wave function, while it is possible to use a larger r_c for the $l=2$ channel than the outermost peak of the all-electron wave function (see Fig. 1). Nonlocal projectors are formed from two $l=0$ and two $l=2$ pseudo-wave-functions. The reference energies for each of the two $l=0$ and two $l=2$ functions are chosen by taking one to be the all-electron eigenvalue and the other to be somewhat higher. The $l=1$ potential is taken as the local potential v_{loc}, since potentials for higher l are much more strongly attractive, leading to possibility of ghost states.[50,51]

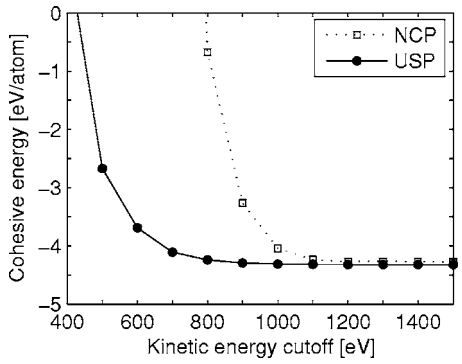

FIG. 2. Convergence of the bulk fcc Cu cohesive energy with respect to the plane-wave energy cutoff for the norm-conserving (NCP) and ultrasoft (USP) Cu pseudopotential.

A corresponding ultrasoft pseudopotential appropriate for plane-wave DFT use is constructed to mimic the behavior of the norm-conserving potential. This is done by constructing pseudo-wave-functions using the same set of parameters (Table I) as those chosen for the norm-conserving potential, except now the norm-conservation constraint of Eq. (35) is released for the two $l=2$ channels. The $l=2$ wave functions are typically much more sharply peaked than those associated with the $l=0$ or $l=1$ channels, and thus relaxing the norm-conservation condition for $l=2$ is essential to yield a reasonably soft pseudopotential. Note that the norm-conservation condition still applies to the $l=0$ and $l=1$ channels, giving a mixed norm-conserving/ultrasoft scheme.[52] In principle, the $l=0$ and $l=1$ channels could have been treated in an ultrasoft fashion as well. However, the choice to leave the norm-conservation constraint in place there is motivated by the desire to mimic as closely as possible its fully norm-conserving partner.

At this point, we depart from standard procedure by defining the charge augmentation function $\tilde{Q}_{ij}^{\mathrm{US}}(\mathbf{r})$ as

$$\tilde{Q}_{ij}^{\mathrm{US}}(\mathbf{r}) = \phi_i^{*\mathrm{NC}}(\mathbf{r})\phi_j^{\mathrm{NC}}(\mathbf{r}) - \phi_i^{*\mathrm{US}}(\mathbf{r})\phi_j^{\mathrm{US}}(\mathbf{r}). \tag{39}$$

This definition differs from the $Q_{ij}^{\mathrm{US}}(\mathbf{r})$ of Eq. (37) in that the reference functions ψ_i have been replaced with the norm-conserving pseudo-wave-functions ϕ_i^{NC}. Consequently, the resulting valence density now reproduces the valence density of the norm-conserving atom, as opposed to that of the all-electron atom. In order to preserve this equivalence, we do not follow the standard practice of pseudizing the augmentation functions $\tilde{Q}_{ij}^{\mathrm{US}}(\mathbf{r})$.

The norm-conserving and ultrasoft Cu pseudopotentials are tested in plane-wave DFT-LDA calculations for bulk fcc Cu. Brillouin zone integrations are done on a $10\times10\times10$ Monkhorst-Pack k-point mesh[53] symmetrized to give 35 irreducible k-points. Total (cohesive) energies are evaluated as $E=E_{\mathrm{bulk}}-E_{\mathrm{atom}}$, where E_{bulk} is the bulk LDA energy per atom and E_{atom} is the LSDA energy of the Cu pseudoatom in the ground state $d^{10}s^1$ configuration. Note that a spin-polarized LSDA treatment of the Cu atom is known to lower the reference atom energy by ~0.2 eV.[54,55] Figure 2 compares the convergence of the bulk fcc Cu cohesive energy with respect to basis set size for both Cu pseudopotentials, and it is evident that the ultrasoft potential converges much more rapidly

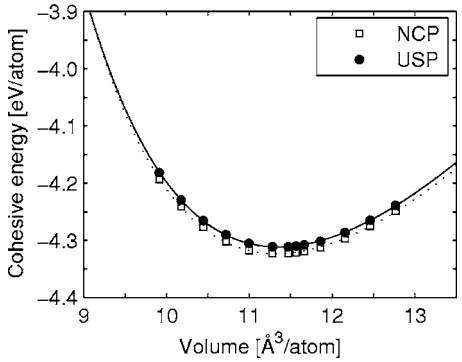

FIG. 3. Equation of state for bulk fcc Cu, fitted to LDA data obtained from norm-conserving (NCP) and ultrasoft (USP) Cu pseudopotentials. Energy differences between the two curves are ~0.01eV.

than its norm-conserving counterpart. The ultrasoft potential does not converge until ~800 eV, which is still quite high for a typical ultrasoft transition metal pseudopotential. This higher kinetic energy cutoff is required because we do not pseudize the augmentation functions $\tilde{Q}_{ij}^{\mathrm{US}}(\mathbf{r})$ to give a softer augmentation charge.

Equilibrium lattice parameter a and bulk moduli B_0 are obtained by the usual procedure of fitting energy versus volume data to Murnaghan's equation of state (Fig. 3).[56] These fit parameters are tabulated in Table II and compared to those obtained from all-electron calculations[57] with LDA exchange-correlation, as well as experimental values. Our LDA values for the lattice parameter a are smaller than the experimental values while the bulk moduli are larger, which is consistent with the well-known tendency of LDA to overbind. The magnitude of the discrepancies between our pseudopotential results and the all-electron calculations is typical of pseudopotential approximations for Cu.[55,58]

III. APPLICATION: Cu(111) DFT-IN-DFT EMBEDDING

In principle, treating both the embedded subsystem and background at the DFT level should give back the same result as that obtained from a DFT calculation for the total system,[32] though this neglects any nonlinearities in the kinetic and exchange-correlation functionals. The embedding theory differs from Kohn-Sham DFT in the treatment of the noninteracting kinetic energy, which is exact in Kohn-Sham DFT. In the embedding theory, however, approximate forms are used for the kinetic energy contribution to the embedding potential. In this section, we compare results from DFT-in-DFT embedding and Kohn-Sham DFT for the total system in order to assess the validity of approximations to the kinetic energy potential. An example of how one can go beyond embedded DFT to explicitly include electron correlation is provided in Sec. IV.

TABLE II. Equilibrium lattice parameter a and bulk moduli B_0 for fcc Cu. Results shown here are obtained from calculations using norm-conserving (NCP) and modified ultrasoft (USP) pseudopotentials. For comparison, results from an all-electron linearized augmented plane-wave (LAPW) calculation are also listed, as well as experimental values.

	a(Å)	B_0 (GPa)
NCP	3.57	170
USP	3.57	168
LAPW[a]	3.52	192
Expt.[b]	3.61	137

[a]Reference 57, using the parameterization of Perdew and Wang (Ref. 72) of the LDA exchange-correlation.
[b]Reference 73.

A test of DFT-in-DFT embedding was done by Klüner *et al.*,[32] who examined a Pd_3 cluster embedded within the Pd(111) surface. We consider here a similar test involving a Cu dimer embedded in the Cu(111) surface, treating both the total system and embedded subsystem with DFT and LDA for exchange-correlation.[40,41] The Cu atoms are represented with the equivalent norm-conserving/ultrasoft pseudopotential pair as discussed in Sec. II B 2. Provided that the exact kinetic energy potential v_{T_s} is known, the electron density in the embedded region should match that of the total system. Here we explore two approximations to v_{T_s}, the Thomas-Fermi λ-von Weizsäcker model, Eq. (17), and the orbital-based model, Eq. (25).

Plane-wave DFT calculations are performed for a four-layer Cu(111) slab, with a 10 Å vacuum layer separating periodic images. The periodic supercell consists of nine Cu atoms per layer and is built from a bulk fcc lattice parameter of 3.57 Å, which corresponds to the equilibrium lattice parameter associated with the Cu pseudopotential (Table II). We do not relax the Cu atom positions, as surface relaxation effects are typically negligible for noble metal (111) surfaces. The plane-wave kinetic energy cutoff is chosen to be 1000 eV, and Brillouin zone integrations are performed on a $5\times5\times1$ Monkhorst-Pack k-point mesh,[53] symmetrized to give five irreducible k-points. Figure 4 shows a cut of the periodic density ρ along a plane passing through the top layer Cu atoms.

We choose the embedded Cu dimer to lie in the top layer of the Cu(111) slab, whose positions are indicated in Fig. 4. The DFT embedded cluster calculations are done with a generally contracted $5s4p4d$ Gaussian basis set derived from all-electron calculations for the Cu atom.[59]

A self-consistent embedding potential v_{emb} is obtained following the procedure described by Klüner *et al.*,[32] which regards the *total* DFT density ρ as frozen. This is in contrast to the scheme given in Sec. II, in which the *background* density ρ_{II} is frozen. At first glance, it would seem reasonable to freeze the total density ρ in DFT-in-DFT embedding, since both the embedded region and background are described with the same level of theory and the same pseudopotential model. However, this is no longer true when one goes beyond a DFT description for the embedded region, and the restriction of a frozen total density ρ is removed in the next example given in Sec. IV.

A DFT calculation using a Gaussian basis set is then performed for the bare Cu dimer. This resulting bare dimer density $\rho_{\mathrm{I}}^{\mathrm{bare}}$ is taken as an initial guess for the embedded dimer density, and with this an initial potential $v_{\mathrm{emb}}[\rho,\rho_{\mathrm{I}}^{\mathrm{bare}}]$ is evaluated. A new density ρ_{I}' is then found in the presence of the $v_{\mathrm{emb}}[\rho,\rho_{\mathrm{I}}^{\mathrm{bare}}]$, and a new potential $v_{\mathrm{emb}}[\rho,\rho_{\mathrm{I}}']$ is con-

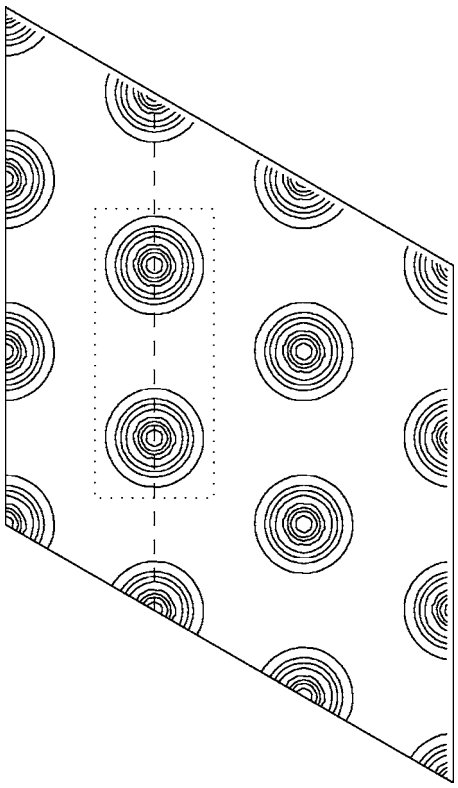

FIG. 4. Cu(111) electron density, viewed along a plane passing through the top layer Cu atoms. The embedded Cu dimer is boxed in dotted lines. The long dashed lines indicate the direction upon which the density plots of Figs. 5 and 6 are viewed.

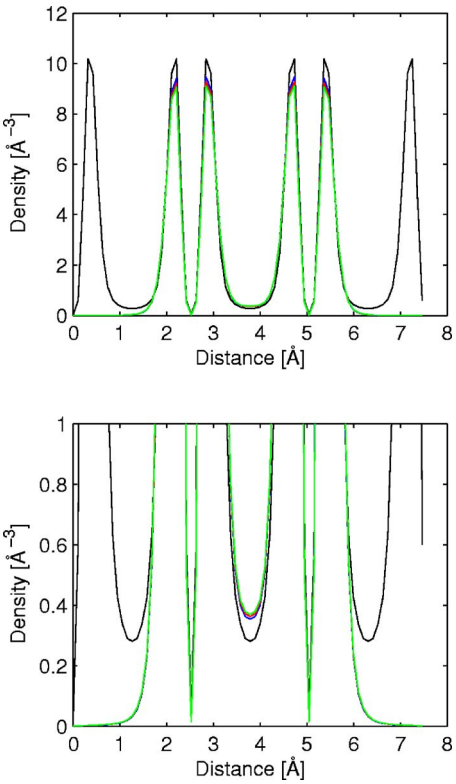

FIG. 5. (Color online) Embedded Cu dimer electron density from the Thomas-Fermi λ-von Weizsäcker kinetic energy potential [Eq. (17)], viewed along the axis passing through the two embedded Cu atoms (Fig. 4). Black lines correspond to plane-wave DFT calculations for the periodic Cu(111) slab, blue for $\lambda=0$, red for $\lambda=1/9$, and green for $\lambda=1/5$. The lower plot represents a magnification of the vertical axis.

structed. The cycle is repeated until a converged, self-consistent embedded cluster density $\hat{\rho}_{\mathrm{I}}$ and potential $v_{\mathrm{emb}}[\rho,\hat{\rho}_{\mathrm{I}}]$ are obtained.

The problem with the approach outlined above is that it is numerically unstable, and this instability can be traced to the contribution from the kinetic energy potential v_{T_s}. Both the von Weizsäcker potential, Eq. (21), and the orbital-based potential, Eq. (25), involve division by a highly nonuniform density. Following Klüner *et al.*,[32] we freeze v_{T_s} to that given by the initial guess for the potential, $v_{T_s}[\rho,\rho_{\mathrm{I}}^{\mathrm{bare}}]$, in order to have a feasible scheme. In this way, only the Hartree v_J and exchange-correlation v_{xc} potentials are allowed to update in the self-consistency cycle.

Figures 5 and 6 show the embedded dimer density, along the direction indicated in Fig. 4. For comparison, the total periodic density is also drawn (solid black). In principle, these quantities should match in the embedded region if the exact kinetic energy potential is used. It can be seen that the various approximations to v_{T_s} do reproduce the essential features of the density. In both the Thomas-Fermi λ-von Weizsäcker model and the orbital-based model, the density near the core (upper panels) is somewhat underestimated. This is because in the numerical implementation of both these models, the kinetic energy potential is replaced with a pure Thomas-Fermi potential in the region near the Cu cores, as discussed in Sec. II A 1. At the low-density interstitial regions (lower panels), the dimer density from the Thomas-Fermi λ-von Weizsäcker potential somewhat underestimates the structure, while dimer density from the orbital-based potential agrees well with the total density ρ for a choice of $\gamma=4/5$.

The Cu(111) embedding results reported here are based on a kinetic energy potential fixed at $v_{T_s}[\rho,\rho_{\mathrm{I}}^{\mathrm{bare}}]$, the potential associated with the bare Cu dimer. Nevertheless, this test case is useful in exploring the role of the kinetic energy potential, and we see that reasonable results for the density can still be obtained from simple models. In the next section, we describe an improved embedding procedure which relaxes the constraints imposed here on v_{T_s}, allowing for a fully self-consistent embedding potential.

IV. APPLICATION: Co/Cu(111) CI-IN-DFT EMBEDDING

The local electronic structure of a magnetic Co adatom on nonmagnetic Cu(111) poses interesting challenges for theory. Scanning tunneling microscopy (STM) experiments find a sharp (~0.01 eV) resonance near the Fermi level ϵ_F of the differential conductance spectrum, localized within ~10 Å from the Co adatom.[34,35] Similar trends have also been seen for a variety of first-row transition metal atoms on noble metal surfaces.[60–62] These experiments have been interpreted within the framework of the Anderson model in the local moment regime.[63–66] In this picture, the resonance near ϵ_F is attributed to a so-called Kondo state, in which the conduction electrons of the bulk metal align their spins to screen out the localized moment on the magnetic atom.

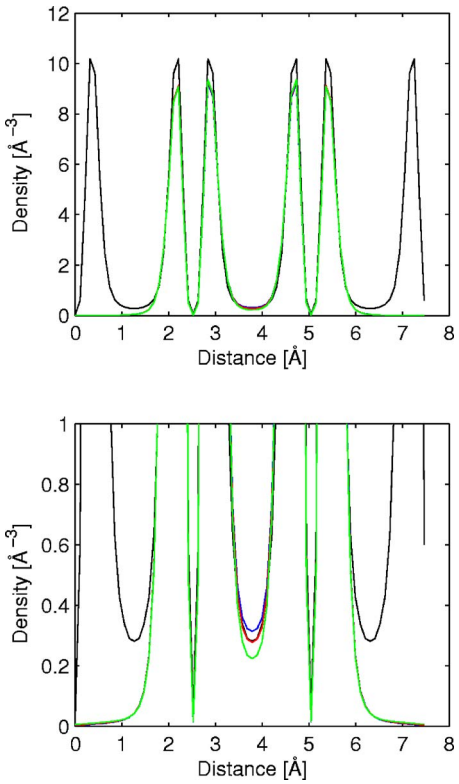

FIG. 6. (Color online) Embedded Cu dimer electron density from the orbital-based kinetic energy potential [Eq. (25)], viewed along the axis passing through the two embedded Cu atoms (Fig. 4). Black lines correspond to plane-wave DFT calculations for the periodic Cu(111) slab, blue for $\gamma=3/5$, red for $\gamma=4/5$, and green for $\gamma=1$. The lower plot represents a magnification of the vertical axis.

It is known that a mean-field treatment of the Anderson model in the local moment regime does not yield the correct ground state, and an accurate description of the Kondo state requires an explicit inclusion of many-body electron correlation effects.[33] Since DFT only accounts for correlation in an averaged sense with approximate functionals, a routine application of DFT is expected to fail in this respect. While modern hybrid functionals which mix in some fraction of Hartree-Fock exchange (e.g., B3LYP) often yield "chemical accuracy" for molecules and insulating systems, these functionals are not well founded for metallic crystals, where Hartree-Fock theory is known to diverge.[67] Therefore, the vast majority of DFT calculations for metals today are still done with the LDA or generalized gradient approximation (GGA) for exchange-correlation.

On the other hand, correlated *ab initio* quantum chemistry methods scale prohibitively with system size and cannot treat extended metal crystals. Our embedding theory, however, can in principle take into account the essential physics: the electron correlation effects localized near the Co adatom and long-ranged electron-electron and electron-ion effects due to a periodic background. The approach we take here is to apply configuration interaction (CI)-based methods to the cluster region of interest, embedded in a self-consistently optimized effective periodic background potential derived from DFT.

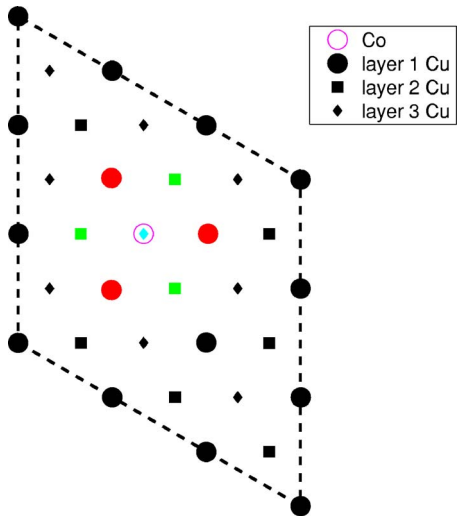

FIG. 7. (Color online) Periodic DFT supercell geometry and atom positions for Co/Cu(111), viewed down along the surface normal. Background atoms are drawn in black, and embedded $CoCu_7$ cluster atoms are colored. The top three Cu layers are shown here; from this view the fourth layer is blocked by the top layer and is not visible.

A. Plane-wave DFT

We begin with spin-polarized, plane-wave DFT calculations for Co on Cu(111) to obtain a periodic total system density ρ using the local spin density approximation (LSDA) for exchange-correlation.[40,41] The plane-wave basis set is truncated at a kinetic energy cutoff value of 800 eV, and the modified ultrasoft pseudopotential described in Sec. II B is used to represent the Cu atoms. The periodic supercell, shown in Fig. 7, is built from the same four-layer Cu(111) slab from Sec. III. A single Co atom is placed in a threefold fcc hollow site, which is the minimum energy site. The positions of the Co and the top two layers of Cu are allowed to relax until the magnitudes of all forces acting on these atoms were less than 0.05 eV/Å.

In the opposite regime, we examine isolated clusters of $CoCu_n$ $(n=3,7)$ removed from the relaxed, periodic Co/Cu(111) slab. The resulting density is also needed to construct a background density ρ_{II} for the embedding calculations of Sec. IV B. Co and Cu have 9 and 11 valence electrons, respectively, and therefore we choose clusters containing odd numbers of Cu atoms so that the total electron count is even. This is to allow for the possibility of a singlet, which we expect for the Kondo ground state. The $CoCu_3$ cluster consists of Co and the three nearest-neighbor Cu atoms of the threefold fcc hollow site, while the $CoCu_7$ cluster includes three additional Cu atoms from the second layer and one Cu atom from the third layer (Fig. 7). Spin-polarized, plane-wave DFT calculations similar to those for Co/Cu(111) are done, except that the supercell here is constructed such that the cluster centers are separated from their neighboring periodic images by ~15 Å of vacuum along all directions.

For both the bare cluster and periodic crystal, we find a ground state with a net magnetic moment of $\sim 2\mu_B$ localized on the Co adatom (Table III). While some spin density can be seen on neighboring Cu atoms in the case of the smallest

TABLE III. DFT magnetic moments (μ_B) for bare $CoCu_n$ ($n=3,7$) and the bulk Co/Cu(111) slab. The heading "layer-1 n.n." refers to the nearest-neighbor Cu atoms in the fcc hollow site upon which the Co adatom resides, and "layer-2 n.n." denotes the nearest-neighbor Cu atoms in the layer below.

	Co	Cu layer-1 n.n.	Cu layer-2 n.n.
Bare $CoCu_3$	1.76	−0.28	···
Bare $CoCu_7$	2.32	0.10	0.12
Co/Cu(111)	2.08	−0.04	0.0

TABLE IV. Low-lying states of the $CoCu_3$ cluster. The upper entries give the bare cluster results relative to the bare cluster $^1A_1$ ground state, while the lower entries give the embedded cluster results relative to the embedded cluster $^1A_1$ ground state.

Term	CAS(12/9) (eV)	MRSDCI (eV)
$^3A_1$ (bare)	0.15	0.06
$^1A_1$	0.0	0.0
$^3A_1$ (embedded)	1.20	1.48
$^1A_1$	0.0	0.0

cluster, $CoCu_3$, this vanishes in the limit of the infinite (111) surface. The DFT ground state we find for Co/Cu(111) is consistent with a mean-field treatment of the Anderson model in the local moment regime. This is not surprising, since Kohn-Sham DFT only takes electron correlation into account in a mean-field sense. On the other hand, it is known that the true ground state of the Anderson model should be spin compensated,[33] and in this case the Cu *s* electrons should somehow quench the magnetic moment localized on the Co. This discrepancy can be attributed to the mean-field nature of Kohn-Sham DFT and the use of approximate exchange-correlation functionals, which are not guaranteed to capture all important electron correlation effects.

B. Correlated wave functions

Electron correlation effects in the $CoCu_n$ cluster are explicitly dealt with using *ab initio* configuration interaction (CI)-based methods. Note that unlike the plane-wave DFT work, the Co and Cu core electrons in $CoCu_n$ should now be represented with pseudopotentials derived from Hartree-Fock theory, and not DFT pseudopotentials that are unscreened with approximate DFT exchange-correlation. Thus, Hay-Wadt large-core effective core potentials (ECPs) are utilized instead, along with their corresponding optimized Gaussian-type basis sets.[44] These ECPs are constructed for 11 and 9 valence electrons of each Cu and Co atom, respectively, consistent with the pseudopotentials employed in the plane-wave DFT calculations.

Existing methods for the optimization of multiconfigurational wave functions are nonlinear in nature, and therefore a good starting guess for the wave function is critical. We obtain an initial set of molecular orbitals from DFT-LDA calculations for bare $CoCu_n$. The DFT molecular orbitals are used as a starting orbital basis for the complete active space, self-consistent field (CASSCF) method,[68,69] which involves a full CI SCF calculation within some prespecified orbital subspace ("active space").

The $CoCu_n$ clusters chosen here have C_{3v} symmetry, which is a non-Abelian group, and thus care must be taken in the CASSCF optimization to avoid problems with symmetry breaking. Orbital rotations are restricted to those within the same irreducible representation, and states with *E* symmetry are optimized by averaging over the two degenerate CI roots in order to avoid loss of equivalence.

For $CoCu_3$, the active space is spanned by the Co $3d4s$ and Cu $4s$ orbitals to give 12 valence electrons distributed over nine active orbitals, i.e., a CAS(12/9) calculation. The 15 Cu $3d$ orbitals are assumed to be doubly occupied (inactive). A similar choice for the $CoCu_7$ active space would lead to a CAS(16/13) which is unnecessarily large and unwieldy for use in the embedding (see below). The size of this active space is reduced by first assuming that two valence electrons doubly occupy an inactive orbital formed from a totally symmetric combination of all $4s$ orbitals, resulting in a CAS (14/12) active space. Such a CAS(14/12) calculation was done for the bare $CoCu_7$ singlet and triplet, and an examination of the natural orbitals reveals three orbitals with negligible occupations (less than ~0.05), indicating that configurations which involve excitations into these orbitals do not contribute significantly to the CASSCF wave function. Thus, we exclude these three orbitals from the active space, and all $CoCu_7$ CASSCF results reported here are obtained from a CAS(14/9) active space.

Dynamical correlation effects can be included by following the CASSCF calculations with multireference singles and doubles CI (MRSDCI),[70,71] in which all single and double excitations out of some prespecified set of reference configurations are included in the CI expansion. For $CoCu_n$, the optimized orbital basis set is taken from the preceding CASSCF calculation, and the resulting configurations whose CI coefficients have a magnitude $\geqslant 0.05$ are used as references for the MRSDCI. Again, the subspace spanned by the Cu $3d$ orbitals (15 for $CoCu_3$ and 35 for $CoCu_7$) is frozen, i.e., they are doubly occupied in all configurations of the CI expansion, leaving 12 correlated electrons for $CoCu_3$ and 16 for $CoCu_7$. States with *E* symmetry are optimized by averaging over the two degenerate CI roots in order to avoid loss of equivalence.

The embedding theory is applied to take into account the effects of the periodic background. An estimate for the background density ρ_{II} is first obtained as $\rho_{II}=\rho-\rho_I^{bare}$, where ρ and ρ_I^{bare} come from plane-wave DFT calculations for the total system and isolated cluster, respectively (Sec. IV A). The CASSCF method is applied to the embedded cluster, whose ions are modeled with *ab initio* Hay-Wadt ECPs. Unlike the DFT-in-DFT example in the previous section, the embedded region is now treated at a level of theory beyond DFT. Therefore, we adopt the scheme described in Sec. II for obtaining a fully self-consistent embedding potential, in which the background density ρ_{II} is regarded as fixed. Once a converged, self-consistent potential v_{emb} is obtained at the CASSCF level, MRSDCI calculations of the ground and excited states are subsequently performed for the embedded cluster in the presence of this v_{emb}. In the MRSDCI, the one-electron potential v_{emb} is transformed to the molecular

orbital basis, along with all the other one-electron matrix elements of the Hamiltonian.

We point out that the embedding potential v_{emb} is assumed to be spin independent here, despite the fact that the total DFT density ρ is derived from spin-dependent LSDA. This is reasonable considering that the Kondo state should be localized, so beyond the range of the local correlation effects we wish to capture with the embedding theory, the Cu(111) surface should be nonmagnetic. Plane-wave DFT calculations for the total Co/Cu(111) system indicate that the background spin density is essentially zero (Table III). Within the embedded region, we expect a large cancellation in the potential, which consists of differences of the form $v[\rho] - v[\rho_I]$, leaving only the nonlinear contributions to v. A spin-independent v_{emb} is also desirable from a technical standpoint. CI-based methods work with configuration state functions (CSFs) that are constructed to be eigenfunctions of S^2, where S is the total electron spin, and it is not straightforward to apply a spin-dependent v_{emb} to a many-body wave function expanded in terms of CSFs.

C. Results

The CASSCF and MRSDCI results for the energetics of bare and embedded $CoCu_n$ clusters are summarized in Tables IV and V. The ground state of bare $CoCu_3$ is a singlet ($^1A_1$) and we find that the effect of the embedding increases the singlet-triplet splitting by over 1 eV. However, as STM experiments have measured the Kondo resonance at distances up to 10 Å away from the adatom center,[34] the $CoCu_3$ cluster is probably much too small to provide a good description of the local electronic structure around the Co adatom, and a frozen DFT background is not expected to account for the strong correlations outside the embedded cluster.

CASSCF and MRSDCI calculations for the larger $CoCu_7$ reveal qualitative differences from $CoCu_3$. The bare $CoCu_7$ ground state is a triplet ($^3A_2$), and the lowest excitations are purely density fluctuations in nature, i.e., they have the same spin multiplicity as the ground state. The singlet is, in fact, a high-energy excited state. A singlet ($^1A_1$) ground state only emerges when the embedding is included, and the lowest excitations now involve spin fluctuations. The singlet-triplet splitting decreases by an order of magnitude from that seen in embedded $CoCu_3$, and it is reasonable to assume that the singlet-triplet splitting would continue to decrease as the cluster size increases. Unfortunately, treating a larger cluster would be prohibitively expensive for CASSCF and MRSDCI. This is also true for the plane-wave DFT calculations of the total system, since the DFT unit cell would have to be increased laterally to prevent interactions with the periodic images of the embedded cluster.

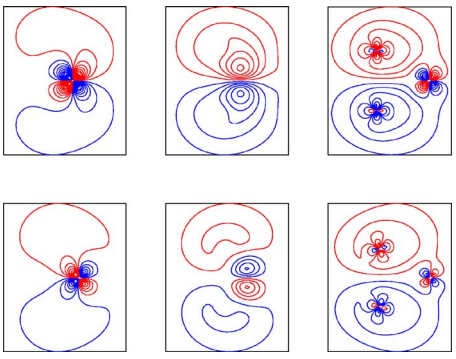

FIG. 8. (Color online) Three slices through the embedded $CoCu_7$ cluster natural orbitals φ_{1e} (upper panels) and φ_{2e} (lower panels) for the $^1A_1$ ground state. Only one member of each doubly degenerate pair is shown. The contour slices are taken along planes parallel to the Cu(111) slab, passing through the Co atom (left), the embedded Cu in the top layer (right), and halfway between these two planes (middle). Red contour lines indicate regions of positive amplitude, while blue denotes regions of negative amplitude. Co–Cu metal-metal bonding between Co d and Cu s is evident.

TABLE V. Low-lying states of the $CoCu_7$ cluster. The upper entries give the bare cluster results relative to the bare cluster $^3A_2$ ground state, while the lower entries give the embedded cluster results relative to the embedded cluster $^1A_1$ ground state.

Term	CAS(14/9) (eV)	MRSDCI (eV)
^1E (bare)	0.85	0.65
^5E	0.60	0.28
^3E	0.08	0.12
$^3A_1$	0.05	0.09
$^3A_2$	0.0	0.0
^1E (embedded)	0.38	0.34
^5E	0.19	0.29
$^3A_1$	0.17	0.24
$^1A_1$	0.0	0.0

An examination of the optimized, ground state CASSCF wave function for the embedded $CoCu_7$ cluster reveals that the strongest correlation effects are due to four electrons, distributed over two sets of doubly degenerate orbitals which transform as the e representation of the C_{3v} point group. These orbitals are denoted as $\{\varphi_{1e}, \varphi_{1e'}\}$ and $\{\varphi_{2e}, \varphi_{2e'}\}$, and contour plots of cuts along planes parallel to the slab are shown in Fig. 8. The multiconfigurational character of the $^1A_1$ ground state is summarized in Table VI, which lists the important configurations present in the CI expansion. The many-body ground state is a superposition of both open- and closed-shell configurations, in contrast to the Anderson model. A conventional treatment of the Anderson model, which assumes a singly occupied impurity (i.e., the local moment regime), thus provides only a partial picture of the true ground state. Instead, we find that the quenching of the impurity moment to produce a singlet ground state is due to chemical bonds forming between the Co d orbitals and the nearest-neighbor Cu s orbitals, as clearly seen in Fig. 8.

V. SUMMARY

We have presented advances made in a density-based embedding theory for crystalline, metallic systems. Our ap-

TABLE VI. Multiconfigurational character of the embedded $CoCu_7$ cluster ground state ($^1A_1$) wave function. Only configurations with CI weights greater than 0.1 are shown here.

Configuration	CI weight
$(\varphi_{1e})^2(\varphi_{1e'})^2$	0.43
$(\varphi_{1e})^2(\varphi_{2e'})^2+(\varphi_{1e'})^2(\varphi_{2e})^2$	0.15
$(\varphi_{1e'})^1(\bar{\varphi}_{1e})^1(\varphi_{2e})^1(\bar{\varphi}_{2e'})^1$	0.14

proach builds upon the work developed in Refs. 28–32, which is based on an approximate embedding potential derived from DFT. First, we have shown how one can employ ultrasoft pseudopotentials in the plane-wave DFT calculations for the total system, in a way which is consistent with the *ab initio* calculations for the embedded cluster. For transition metals, this has the effect of significantly reducing the computational effort needed for plane-wave DFT. Second, our embedding model starts with a DFT estimate for the background density $\rho_{\mathrm{II}}=\rho-\rho_{\mathrm{I}}^{\mathrm{bare}}$, which is held fixed. In contrast to previous efforts, the theory now provides a locally corrected *total* density $\hat{\rho}=\hat{\rho}_{\mathrm{I}}+\rho_{\mathrm{II}}$, where $\hat{\rho}_{\mathrm{I}}$ is the self-consistent density of the embedded cluster in the presence of the embedding potential v_{emb}. This new approach also eliminates the numerical difficulties involved in finding a fully self-consistent potential v_{emb} which plagued earlier work.[28–32] And finally, while v_{emb} is obtained at the CASSCF level, we improve on the description of the embedded region with MRSDCI theory, which takes into account dynamical correlation effects not included in CASSCF. These advances in the methodology make the embedding theory an important tool for the accurate study the electronic structure of strongly correlated systems.

The embedding theory was applied to two examples. The first was a test case involving a Cu dimer embedded in Cu(111), where both the embedded region and total system were treated with DFT. The purpose behind this test was to explore model forms for the kinetic energy potential, a key approximation in our theory. We showed in this example that simple models for the kinetic energy potential yield densities that reproduce reasonably well those from Kohn-Sham (exact kinetic energy) calculations. The second example considered the adsorption of Co on Cu(111), which is a strongly correlated system exhibiting the Kondo effect. It is known that the inclusion of many-body correlation effects is necessary to obtain the correct ground state; however, this has so far only been done in the context of parametrized models. Our application here is a first principles effort, and we demonstrate how the embedding theory can successfully yield the Kondo ground state, in contrast to standard DFT approaches. We therefore expect that this self-consistent embedded CI theory holds promise for the treatment of other localized many-body correlation effects in condensed matter.

ACKNOWLEDGMENTS

The authors thank Peter Nordlander, Niri Govind, and Thorsten Klüner for useful discussions, Accelrys, Inc. for providing the CASTEP code, Roland Lindh for help with the MOLCAS code, and Andrew Szilva for implementing Hay-Wadt ECPs in MOLCAS. This work was supported by a grant from the Department of Energy Basic Energy Sciences. One of the authors (P.H.) also acknowledges partial support from a California NanoSystems Institute postdoctoral fellowship.

[1] P. Hohenberg and W. Kohn, Phys. Rev. **136**, B864 (1964).
[2] W. Kohn and L. J. Sham, Phys. Rev. **140**, A1133 (1965).
[3] J. Sauer, Chem. Rev. (Washington, D.C.) **89**, 199 (1989).
[4] J. L. Whitten and H. Yang, Surf. Sci. Rep. **24**, 55 (1996).
[5] A. Redondo, W. A. Goddard III, T. C. McGill, and G. T. Surratt, J. Vac. Sci. Technol. **20**, 733 (1976).
[6] A. Redondo and W. A. Goddard III, J. Vac. Sci. Technol. **21**, 344 (1982).
[7] C. J. Wu and E. A. Carter, Phys. Rev. B **45**, 9065 (1992).
[8] P. Nachtigall, K. D. Jordan, and K. C. Janda, J. Chem. Phys. **95**, 8652 (1991).
[9] R. Konečný and D. J. Doren, J. Chem. Phys. **106**, 2426 (1996).
[10] N. W. Winter, R. M. Pitzer, and D. K. Temple, J. Chem. Phys. **86**, 3549 (1987).
[11] N. W. Winter, R. M. Pitzer, and D. K. Temple, J. Chem. Phys. **87**, 2945 (1987).
[12] C. Pisani, Phys. Rev. B **17**, 3143 (1978).
[13] C. Pisani, R. Dovesi, and P. Carosso, Phys. Rev. B **20**, 5345 (1979).
[14] S. Krüger, U. Birkenheuer, and N. Rösch, J. Electron Spectrosc. Relat. Phenom. **69**, 31 (1994).
[15] S. Krüger and N. Rösch, J. Phys.: Condens. Matter **6**, 8149 (1994).
[16] C. Pisani, R. Dovesi, C. Roetti, M. Causà, R. Orlando, S. Casassa, and V. R. Saunders, Int. J. Quantum Chem. **77**, 1032 (2000).
[17] J. L. Whitten and T. A. Pakkanen, Phys. Rev. B **21**, 4357 (1980).
[18] J. L. Whitten, Phys. Rev. B **24**, 1810 (1981).
[19] J. D. Head and S. J. Silva, J. Chem. Phys. **104**, 3244 (1996).
[20] U. Gutdeutsch, U. Birkenheuer, S. Krüger, and N. Rösch, J. Chem. Phys. **106**, 6020 (1997).
[21] U. Gutdeutsch, U. Birkenheuer, and N. Rösch, J. Chem. Phys. **109**, 2056 (1998).
[22] P. Cortona, Phys. Rev. B **44**, 8454 (1991).
[23] T. A. Wesolowski and A. Warshel, J. Phys. Chem. **97**, 8050 (1993).
[24] J. Neugebauer, M. J. Louwerse, and E. J. Baerends, J. Chem. Phys. **122**, 094115 (2005).
[25] J. Neugebauer, C. R. Jacob, T. A. Wesolowski, and E. J. Baerends, J. Phys. Chem. A **109**, 7805 (2005).
[26] E. V. Stefanovich and T. N. Truong, J. Chem. Phys. **104**, 2946 (1996).
[27] N. Choly, G. Lu, W. E, and E. Kaxiras, Phys. Rev. B **71**, 094101 (2005).
[28] N. Govind, Y. A. Wang, A. J. R. da Silva, and E. A. Carter, Chem. Phys. Lett. **295**, 129 (1998).
[29] N. Govind, Y. A. Wang, and E. A. Carter, J. Chem. Phys. **110**, 7677 (1999).
[30] T. Klüner, N. Govind, Y. A. Wang, and E. A. Carter, Phys. Rev. Lett. **86**, 5954 (2001).
[31] T. Klüner, N. Govind, Y. A. Wang, and E. A. Carter, Phys. Rev. Lett. **88**, 209702 (2002).
[32] T. Klüner, N. Govind, Y. A. Wang, and E. A. Carter, J. Chem. Phys. **116**, 42 (2002).
[33] A. C. Hewson, *The Kondo Problem to Heavy Fermions*, Cambridge Studies in Magnetism Vol. 2 (Cambridge University Press, Cambridge, 1993).
[34] H. C. Manoharan, C. P. Lutz, and D. M. Eigler, Nature (London) **403**, 512 (2000).
[35] N. Knorr, M. A. Schneider, L. Diekhöner, P. Wahl, and K. Kern, Phys. Rev. Lett. **88**, 096804 (2002).
[36] M. D. Segall, P. J. D. Lindan, M. J. Probert, C. J. Pickard, P. J. Hasnip, S. J. Clark, and M. C. Payne, J. Phys.: Condens. Matter **14**, 2717 (2002).
[37] G. Karlström, R. Lindh, P.-Å. Malmqvist *et al.*, Comput. Mater. Sci. **28**, 222 (2003).
[38] R. G. Parr and W. Yang, *Density-Functional Theory of Atoms and Molecules*, International Series of Monographs on Chemistry Vol. 16 (Oxford University Press, New York, 1989).
[39] K. Yonei and Y. Tomishima, J. Phys. Soc. Jpn. **20**, 1051 (1965).
[40] D. M. Ceperley and B. J. Alder, Phys. Rev. Lett. **45**, 566 (1980).
[41] J. P. Perdew and A. Zunger, Phys. Rev. B **23**, 5048 (1981).
[42] L. E. McMurchie and E. R. Davidson, J. Comput. Phys. **44**, 289 (1981).
[43] C.-K. Skylaris, L. Gagliardi, N. C. Handy, A. G. Ioannou, S. Spencer, A. Willetts, and A. M. Simper, Chem. Phys. Lett. **296**, 445 (1998).
[44] P. J. Hay and W. R. Wadt, J. Chem. Phys. **82**, 270 (1985). In this reference, there is a sign error in the Cu ECP parameters. In Table III, the last line of the Cu entry for the $d-f$ potential, the value of d_k should be −0.462 168 0, not 0.462 168 0.
[45] G. B. Bachelet, D. R. Hamann, and M. Schlüter, Phys. Rev. B **26**, 4199 (1982).
[46] N. Troullier and J. L. Martins, Phys. Rev. B **43**, 1993 (1991).
[47] D. Vanderbilt, Phys. Rev. B **41**, 7892 (1990).
[48] K. Laasonen, A. Pasquarello, R. Car, C. Lee, and D. Vanderbilt, Phys. Rev. B **47**, 10142 (1993).
[49] P. E. Blöchl, Phys. Rev. B **41**, 5414 (1990).
[50] X. Gonze, P. Käckell, and M. Scheffler, Phys. Rev. B **41**, 12264 (1990).
[51] X. Gonze, R. Stumpf, and M. Scheffler, Phys. Rev. B **44**, 8503 (1991).
[52] K. Stokbro, Phys. Rev. B **53**, 6869 (1996).

[53] H. J. Monkhorst and J. D. Pack, Phys. Rev. B **13**, 5188 (1976).
[54] P. H. T. Philipsen and E. J. Baerends, Phys. Rev. B **54**, 5326 (1996).
[55] M. Fuchs, M. Bockstedte, E. Pehlke, and M. Scheffler, Phys. Rev. B **57**, 21346 (1998).
[56] F. D. Murnaghan, Proc. Natl. Acad. Sci. U.S.A. **30**, 244 (1944).
[57] A. Khein, D. J. Singh, and C. J. Umrigar, Phys. Rev. B **51**, 4105 (1995).
[58] G. Kresse and J. Hafner, J. Phys.: Condens. Matter **6**, 8245 (1994).
[59] K. Pierloot, B. Dumez, P.-O. Widmark, and B. O. Roos, Theor. Chim. Acta **90**, 87 (1995).
[60] J. Li, W.-D. Schneider, R. Berndt, and B. Delley, Phys. Rev. Lett. **80**, 2893 (1998).
[61] V. Madhavan, W. Chen, T. Jamneala, M. F. Crommie, and N. S. Wingreen, Science **280**, 567 (1998).
[62] T. Jamneala, V. Madhavan, W. Chen, and M. F. Crommie, Phys. Rev. B **61**, 9990 (2000).
[63] O. Ujsaghy, J. Kroha, L. Szunyogh, and A. Zawadowski, Phys. Rev. Lett. **85**, 2557 (2000).
[64] A. Schiller and S. Hershfield, Phys. Rev. B **61**, 9036 (2000).
[65] M. Plihal and J. W. Gadzuk, Phys. Rev. B **63**, 085404 (2001).
[66] G. A. Fiete and E. J. Heller, Rev. Mod. Phys. **75**, 933 (2003).
[67] N. W. Ashcroft and N. D. Mermin, *Solid State Physics* (Brooks-Cole, Belmont, MA, 1976).
[68] B. O. Roos, P. R. Taylor, and P. E. M. Siegbahn, Chem. Phys. **48**, 157 (1980).
[69] B. O. Roos, in *Lecture Notes in Quantum Chemistry*, Lecture Notes in Chemistry Vol. 38, edited by B. O. Roos (Springer-Verlag, Berlin, 1992), p. 177.
[70] H.-J. Werner and P. J. Knowles, J. Chem. Phys. **89**, 5803 (1988).
[71] P. E. M. Siegbahn, in *Lecture Notes in Quantum Chemistry*, Lectures Notes in Chemistry Vol. 58, edited by B. O. Roos (Springer-Verlag, Berlin, 1992), p. 255.
[72] J. P. Perdew and Y. Wang, Phys. Rev. B **45**, 13244 (1992).
[73] C. Kittel, *Introduction to Solid State Physics*, 7th ed. (Wiley, New York, 1996).